Laboratory scale testing of ignition overpressure for space vehicle launch pad environments

Charles E. Tinney[*], John A. Valdez[†], and Hayley Meier[‡]

The University of Texas at Austin, Austin, TX 78713, USA

Joseph H. Ruf[§]

NASA Marshall Space Flight Center, Huntsville, Alabama 35812

A scale model of a NASA representative space vehicle is used to develop a refined estimate of the transient pressure loads that are expected to form at the base of the vehicle in the event of a vapor cloud explosion. Flammable vapor clouds are known to form prior to engine startup due to the significant amount of unburned hydrogen that is ejected from the combustion chamber. In the event of a vapor cloud explosion, the vehicle and payload must be able to withstand the resulting overpressure waves. The study comprises an array of pressure sensors located along the base heat shield of the scale model space vehicle as well as the interior wall and throat plug plane of the solid rocket booster. A spark source generator is used to simulate the overpressure wave produced by a vapor cloud explosion while measurements are acquired with and without the effect of a mobile launcher. Time-resolved schlieren images of the simulated vapor cloud explosion reveal the path and impact of both the initial wave and several reflected waves on the various components at the base of the space vehicle. In some instances, the reflected waves superpose to create waves that are higher in amplitude than the initial overpressure wave. A time frequency analysis of the pressure waveforms measured inside the solid rocket booster reveal a ring down tone corresponding to a standing wave that is four times the length of the nozzle.

I.   Introduction

The Space Launch System (SLS) is NASA's next super heavy-lift expendable space launch vehicle with an anticipated first launch date in 2020. Various configurations are being planned in order to separately transport crew and payload beyond earth orbit. At the onset of the program, every configuration will employ the same core stage comprising four RS-25 engines and two solid rocket boosters (SRB). This RS-25 is a liquid-fuel (oxygen and hydrogen) cryogenic engine that has been in operation for nearly four decades and is what powered the Space Shuttle Orbiter. Like the Space Shuttle Orbiter, the SLS launch sequence will comprise staggered startups of the RS-25 engines followed by startup of the SRBs. During RS-25 engine startup, a significant amount of unburned hydrogen is ejected from the combustion chamber that then mixes with ambient oxygen to form a flammable vapor cloud. At the base of the SLS vehicle, this vapor cloud is at risk of igniting which can result in the formation of an overpressure wave capable of damaging the vehicle and launch pad. For the space shuttle orbiter, the risk was mitigated by installing hydrogen burn-off ignitors (HBOI) below the exit plane of the RS-25 nozzle. HBOIs emit burning metallic particles that immediately burn off any unburned hydrogen thereby preventing large vapor clouds from forming at the base of the vehicle. During the early years of the shuttle program, the placement and orientation of these HBOIs were refined in order to significantly reduce the likelihood of a vapor cloud explosion (VCE). However, in the event that a hydrogen vapor cloud did ignite, the vehicle and launch pad were designed to survive the loads from

American Institute of Aeronautics and Astronautics

the resulting overpressure wave. The same design practices are being required for the SLS vehicle. However, because of the geometrical differences between the SLS and space shuttle vehicles (including different launch pads) a new understanding of these anticipated loads is needed for the SLS vehicle.

The amplitude of the overpressure wave produced by a VCE can be determined in one of three ways. That is, it can be estimated analytically using the TNT equivalence method,[1–3] numerically using modern computational fluid dynamics (CFD),[4] or from direct measurements under carefully controlled conditions.[5] The first of these has been scrutinized for some time now because of the lack of correlation between the quantity of fuel in the VCE and its yield. The primary reason being that the actual blast yield is a consequence of a wide spectrum of combustion modes and not the amount of fuel involved.

Combustion modes are categorized by flame speed which depend on the density and uniformity of the cloud mixture, the state of the flame front (laminar or turbulent) and by secondary effects pertaining to geometrical confinement. In an effort to circumvent problems with the TNT equivalence method, Tang and Baker[1] developed a new set of blast curves for three combustion mode regimes: vapor cloud detonation, supersonic deflagration and subsonic detonation. Their models show that for supersonic flame speeds (the velocity of heat addition in a Lagrangian coordinate system), the relationship between overpressure wave amplitude and source distance collapse to a single curve for locations outside of the vapor cloud where source amplitude decays spherically ($p \propto 1/r$). The same is true for specific impulse of the shock front. Furthermore, negative overpressures never exceed positive overpressures while magnitudes of negative and positive impulse are comparable outside of the combustion zone. On the contrary, where subsonic flame speeds are concerned, Tang and Baker[1] show how the correlation between overpressure wave amplitude decay and source distance do not merge, thereby demonstrating how flame speed, either subsonic or supersonic, greatly effects the blast yield outside of the combustion zone. More recently, the simulations of Allgood,[4] who used CFD-based methods incorporating a multi-species chemical reaction model, showed that in a realistic propulsion test environment, three modes of combustion could be generated and controlled. That is, deflagration, deflagration-to-detonation transition and prompt-detonation. Deflagration-to-detonation transition (from low-speed deflagration to high-speed detonation) is caused by accelerations in flame speed due to turbulence generation, strong pressure gradients generated by nearby reflecting boundaries or combustion instabilities.

For this study, the loads of interest are the ones produced by the overpressure wave emitted by a VCE where the points of interest are located outside of the combustion zone. Therefore, proper classification of the combustion mode or flame speed is not required for the successful outcome of this study. Rather, on account of the geometrical complexities of the vehicle hardware and launch pad, the effort is focused on quantifying the relative amplitudes at various points along the base of the space vehicle where its proximity to the VCE overpressure wave is relevant. Measurements are broken into two primary objectives. The first focuses on characterizing the shape, speed and amplitude of the pressure waveform produced by a simple source in an unconstrained environment. Doing so provides a detailed understanding of the kinds of inputs that one would use to accurately model the measurements reported here. This simple source simulates the overpressure wave produced by vapor cloud explosion and is geometrically scaled to match laboratory scale hardware. The second objective then focuses on measuring the effect of the simple source on a laboratory scaled model of a NASA representative space vehicle. Of particular interest is the pressure load at the center of the vehicle base heat shield (BHS) as well as the throat plug plane of the solid rocket booster.

II.   Test Apparatus

All measurements were conducted at the Applied Research Laboratories at The University of Texas at Austin (ARL-UT). A description of this facility is provided by Valdez and Tinney,[6] Baars and Tinney[7] and Donald *et al.*[8] Measurements comprised three primary pieces of equipment. That is, a spark generator, a combination of 1/8 in. and 1/4 in. microphones and a high speed, high resolution digital optical flow visualization instrument. The spark generator is used to simulate a geometrically scaled vapor cloud explosion while the microphones and optical flow instruments are used to measure it. A description of these three items is as follows.

- The geometrically scale vapor cloud explosion is simulated using a model GTS 51-4 spark generator made by Grozier Technical Systems, Inc. This triggered spark generator comprises a pair of 0.0625 inch diameter tungsten electrodes separated by a small gap which forms an arc when a sufficiently high voltage is applied to the spark gap. The electrode gap is ionized by a 30kV low energy trigger spark which discharges a high voltage capacitor with approximately 15 joules of spark energy. Doing

American Institute of Aeronautics and Astronautics

so produces a spherically shaped acoustic impulse. Several studies can be found in the open literature that describe the shape and amplitude of the waveform produced by this spark generator.[9–12]

- Both 1/8 in. and 1/4 in. microphones were used to measure the pressure waveform produced by this spark generator. All microphone sets are prepolarized pressure field microphones manufactured by G.R.A.S. and are manufacturer calibrated with both microphone and preamplifier combined. The 1/8 in. microphones are type 46DD capsules with type 26CD preamplifiers. Given their small sensing diaphragms (3.2 mm capsules), these microphones are capable of resolving signals over a broad range of frequencies (6.5 Hz to 140 kHz with ± 3 dB error) and dynamic range (52 to 174 dB, reference 20μPa) with a nominal sensitivity around 0.8mV/Pa. As for the 1/4 in. microphones, these are type 40BD capsules with type 26CB preamplifiers (4 Hz to 70 kHz with ± 2 dB error) and have a dynamic range of (44 to 166 dB, reference 20μPa) with a nominal sensitivity around 1.45mV/Pa. IEPE power is provided by way of a Dytran Instruments Inc. 4121 power supply while microphone voltages are recorded simultaneously using four National Instruments PXI-6122 boards. Each PXI-6122 board has four single ended channels that digitize signals at a rate of 500 kHz per channel with 16 bit resolution over ±5v.

- Visualizations of the source and sound field were accomplished using a schlieren/shadowgraph system oriented in a z-type fashion; a discussion of schlieren and shadowgraphy techniques can be found elsewhere.[13–18] The principle elements that make of this system are the light source, a pair of parabolic mirrors, and a digital camera. The light source consists of a LUMINUS CBT-120 Green 510-540nm LED operating continuously at 4.5V and 8A. Light rays are first focused onto a circular aperture using a Nikon 28 mm, 1:2.8 focusing lens which then illuminate two gold coated parabolic mirrors (12.5 inch diameter) with 100 inch focal lengths. Schlieren is achieved by inserting a razor blade cutoff to block portions of the light entering the high speed digital camera. Large fields of view are obtained using a Nikon 36-72mm, 1:3.5 zoom lens whereas narrow fields of view use a Sigma 50-150mm, 1:2.8 zoom lens. High speed images are acquired using a i-SPEED 726 monochromatic camera manufactured by ix Cameras. This camera has a maximum resolution of 2048×1536 pixels that are 13.5μm in length with 12 bit depth and a camera shutter speed of up to 1μs. Full sensor resolution can be captured uninterrupted at a speed of 8,512 frames per second (fps) for 7.6 seconds whereas the maximum speed of 1,000,000 fps is achieved at a reduced resolution of 336×42 pixels and for a 14 second duration. Additional information pertaining to this hardware is provided by Valdez and Tinney.[6]

III.   Source Characterization

An attractive feature of the spark generator is that it produces a reliable and consistent waveform that is easy to generate. Earlier efforts employed firecrackers (often referred to as "flashlight firecrackers") which were found to emit much higher amplitude waveforms but were less consistent and less symmetric. The steeper gradients that result from having higher amplitude pressure waves permit better visualizations and so the firecrackers are used to provide qualitative visuals of the pressure waves that reflect from the various surfaces of the model space vehicle. For now, we will focus on characterizing the shape, speed and amplitude of the pressure wave emitted by this spark generator. These measurements were acquired far from any reflecting surfaces and with the spark generator wand being supported by a camera tripod.

In Fig. 1, a sparse sequence of shadowgraphy images of the pressure wave produced by the spark generator is shown. These images were acquired at a rate of $f_s = 400,000$ frames per second (fps) using a 1μs shutter speed and 200×200 pixel resolution with 2^{12} bit monochromatic dynamic range. It is evident from these images that the spark generator produces a spherically shaped wave. A slice across the center of each image at $y = 0$ is shown immediately below. Due to the insertion of amplitude modulation effects by the digital camera, the amplitude of these extracted waveforms have been normalized by their peak value. If the pressure wave is acoustic, then it should travel at the sound speed, $a_\infty = \sqrt{\gamma RT}$ where $R = 287$ J kg^{-1} K^{-1} is the gas constant, $\gamma = 1.4$ is the ratio of specific heats for air and the temperature in the room is measured to be $T = 295$ K. This equates to a sound speed of $a_\infty = 344$ m/s (1128.6 ft/s). A reference time of $t = 0$ establishes the instant in time when the light flash produced by the spark generator is made visible by the shadowgraphy system. If one assumes that the speed of the wave front is constant, then the expected location where the wavefront should occur in the image is identified by the vertical lines in the extracted waveforms. For the three cases shown, the wavefront is located ahead of the predicted value, thereby suggesting that the

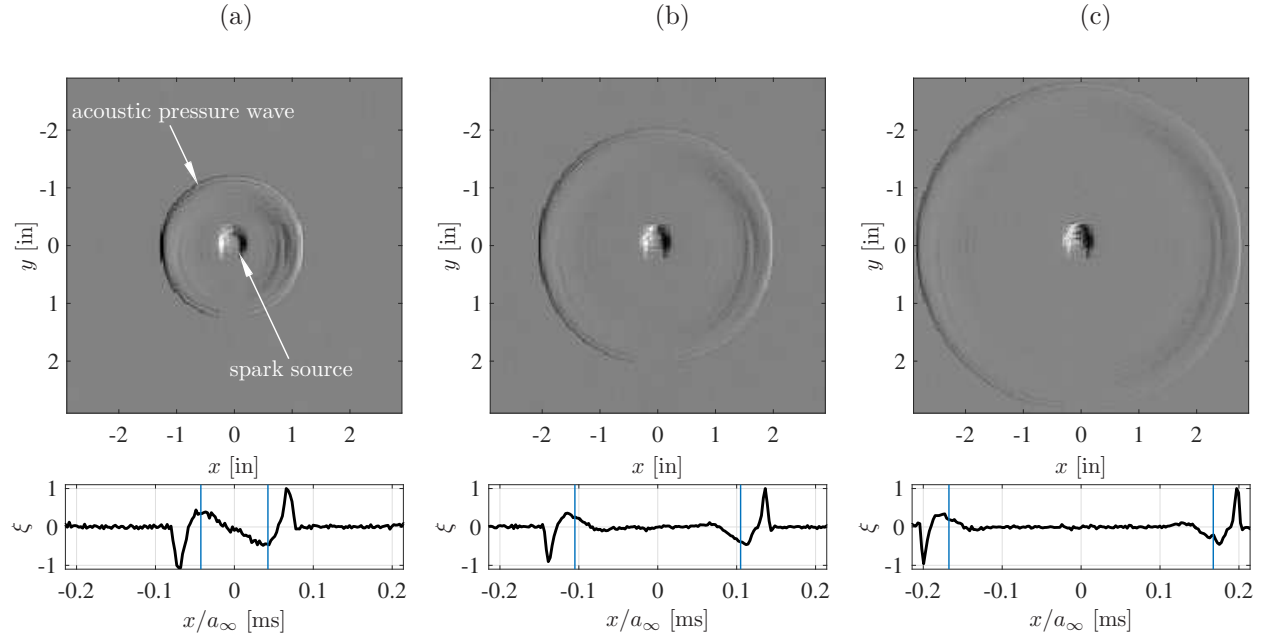initial speed of the wavefront is much faster than a_∞.

Figure 1: Shadowgraphy images of the spark at three instances in time sampled at 400,000 fps. (a) $t = 0.0450$ ms, (b) $t = 0.1075$ ms, and (c) $t = 0.1700$ ms. Vertical lines identify instances in time where the first peak should occur, assuming a constant propagation speed of $a_\infty = 344.3$ m/s.

Closer inspection of the wave speed is presented in Fig. 2a for segments of the wave that are traveling to the right (RHS) and left (LHS) of the spark. Measured displacements are based on the location of the waveform peak. Once again, spark ignition identifies $t = 0$ and $x = 0$. Arrival times are limited by the sampling speed of the camera whereas the location of the peak is confined by the size of the pixel and its resultant image magnification; the image magnification factor for these measurements was determined to be 0.0330 in/pix. In Fig. 2a, both the RHS and LHS wave speeds are nearly identical thereby providing further evidence that this spark source is generating symmetric pressure waveforms. Divergence of these trends yields an estimate of the wave's propagation speed, which is shown in Fig. 2b. Here, the starting speed is nearly two times larger than the sound speed of the ambient gas. At a distance of 2 inches from the source, both RHS and LHS waves decelerate to a wave speed equal to a_∞ and then remain unchanged. It is postulated that the supersonic wave speed is an artifact of the shadowgraphy system and that the true wave speed should be that of the sound speed of the gas. This is confirmed using phased array measurements from a densely packed array of microphones positioned closer to the spark source (not shown).

Raw pressure waveforms are presented in Fig. 3a along with one-sided spectra in Fig. 3b. These waveforms are measured using two of the 1/8 in. microphones placed at grazing incidence to the passing waveform with microphone capsules positioned at the same height as the spark source. Pressure waveforms are sampled at 400 kHz without low pass filters; 1/8 in. microphones are limited by an upper bandwidth of 140kHz. One-sided power spectral densities are computed from 1024 samples which yield a spectral resolution of $df = 390$ Hz. The first microphone (p_1) is located to the left of the spark source at $x_1 = 5.06$ inches (to measure the LHS) whereas the second microphone (p_2) is located to the right of the spark source at $x_2 = 4.41$ inches (to measure the RHS waveform). Waveform amplitudes are scaled to a position at $x = 5$ inches by assuming spherical decay ($p \propto 1/r$). The x-axis in Fig. 3a is presented as a function of time (upper sub figure) and space (lower sub figure). Measurements are repeated with and without grid capsules installed in order to reveal the contaminating effects of the microphone. Fig. 3a reveals an overall waveform length of approximately 1 inch at this location, which coincides with the peak frequency of 10 kHz in Fig. 3b.

The effect of distance on the pressure waveform can be seen in Fig. 4a using a line array of microphones positioned roughly between 10 and 50 inches from the spark source. These measurements were also acquired with microphone diaphragms at grazing incidence to the pressure wave but with grid caps on. Alignment of
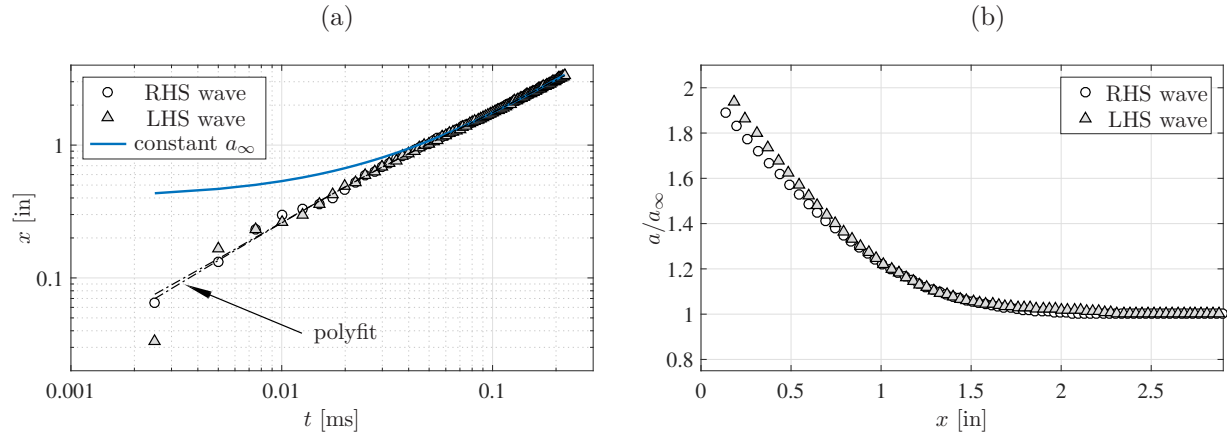
Figure 2: (a) Displacement of the right hand side (RHS) and left hand side (LHS) peak values at sequential instances in time. (b) Wave propagation speed relative to the speed of sound.
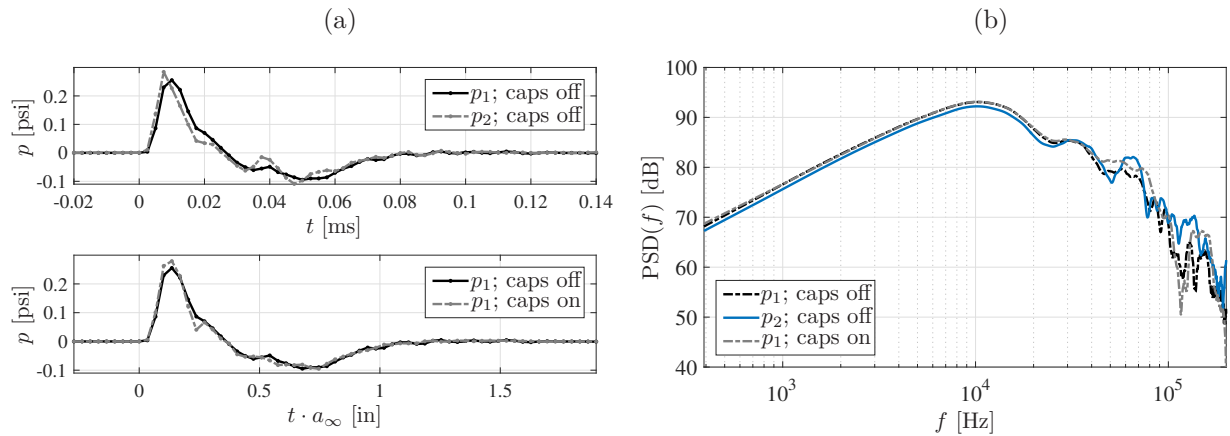

Figure 3: Effect of grid caps on (a) acoustic waveform and (b) power spectral density (PSD) at $x = 5$ inch from spark source.

these waveforms is based on their rising edge. Spreading of the waveform is shown to increase with distance from the source and is an indicator that weak non-linear distortion effects are present. Decay of the peak pressure is shown in Fig. 4b to compare favorably to $p \propto 1/r$ therefore demonstrating how the waveform, at these distances from the source, is spreading spherically.

IV.   Space Vehicle Loads

Having now characterized the speed, shape, amplitude and spectral characteristics of the source, we are interested in understanding the pressure loads on a model scale space vehicle as produced by this simple source. This is accomplished by placing the spark generator below the vehicle as shown in Fig. 5. The vehicle is approximately a 1/30th scale mach-up of the lower stage of a NASA representative space vehicle and comprises four high area-ratio parabolic contour nozzles (denoted PAR-3 in Fig. 5), two SRBs with throat plugs and a space vehicle base heat shield. Both the SRBs and BHS are fabricated from 3D printed material whereas the PAR-3 nozzles are fabricated from aluminum; all components are acoustically reflective. Two different vehicle configurations are studied. One with the space vehicle alone (two SRBs, four RS-25 nozzles and the BHS) as shown in Fig. 5a; the other with the upper mobile launcher (ML) installed, (flame
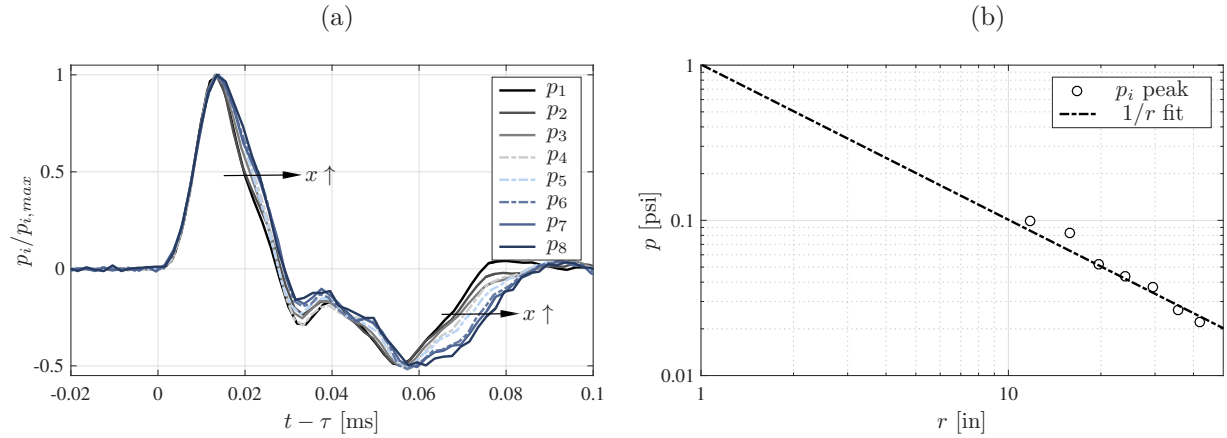
Figure 4: Microphone line array measurements. (a) Pressure waveforms aligned by the rising edge. (b) Peak pressure of arriving waveform compared to spherical decay.

duct and SRB haunches), as shown in Fig. 5b. For each configuration, the spark source is placed at two different locations below the vehicle. The first location is centered on the space vehicle (identified as source 1 in Fig. 5), whereas the second is centered on the RS-25 nozzle lip line (identified as source 2 in Fig. 5). Raw images of the test apparatus with the ML installed is shown in Fig. 6.

A total of 20 pressure sensing ports are used to capture the waveforms at various points along the vehicle and ML using 1/8 in. microphones as shown in Fig. 5. Microphones are mounted so that their protective grids are flush with the vehicle surfaces. Ports 1-5 are located along the side wall of the SRB nozzle, ports 6-10 along the SRB throat plug, ports 11-15 along the vehicle BHS, and ports 17-20 along the walls of the ML duct. Two reference points are considered in this study. One at the center of the SRB throat (port 8) and the other at the center of the BHS (port 16). Scaling of the measured waveforms is accomplished using the sound speed of air and the length of the SRB nozzle (defined by L).

A. Time-resolved Schlieren Imaging

A sparse sequence of images from the schlieren system are shown in Figs. 7 and 8 corresponding to spark source locations 1 and 2, respectively. The location of the schlieren window is shown in Fig. 5 while measurements are confined to the setup without the ML; the ML prevents optical access to the region below the vehicle, which is the primary region of interest in this study. A frame rate of 75,000 fps is used while image contrast is enhanced by inserting a firecracker (grain based explosive) in place of the spark generator. Pressure waves produced by the firecracker are an order of magnitude larger than the spark generator, but are less consistent in shape and acoustic directivity. Evidence of this is shown in Fig. 7a and 8a where the initial wavefront appears to be only partially spherical when compared to the shadowgraphy images of the spark source in Fig. 1. By the time the firecracker generated wavefront impacts vehicle surfaces (Figs. 7b and 8b), its shape is relatively spherical therefore providing a qualitative visual of the initial and reflected waves that are expected to form with the spark generator.

An important feature to point out from these images is the formation of a secondary (reflected) wave, which is first identified in Fig. 7b. This secondary wave is caused by reflection of the initial wave from the PAR-3 nozzles. Because the space vehicle comprises four of these PAR-3 nozzles, and because the spark source in this setup (source location 1) is symmetric with respect to the vehicle BHS and its four PAR-3 nozzles, then four reflected waves (one from each PAR-3 nozzle) will form behind the initial wave, as shown in Fig. 7c-d. These reflecting waves intersect one another to form a node at the center of the vehicle BHS. It will be shown how these reflected waves can produce pressure footprints on the space vehicle of equal or greater strength relative to the initial wave. It is evident from Fig. 7e-g that the initial wavefront is allowed to propagate up the vehicle between the space vehicle body and the SRB. Several reflecting waves also form from the thermal curtain of the SRB and demonstrate the complexity of the reflected wavefronts that form in this environment. Similar kinds of waves are observed in Fig. 8 for the second spark source location.
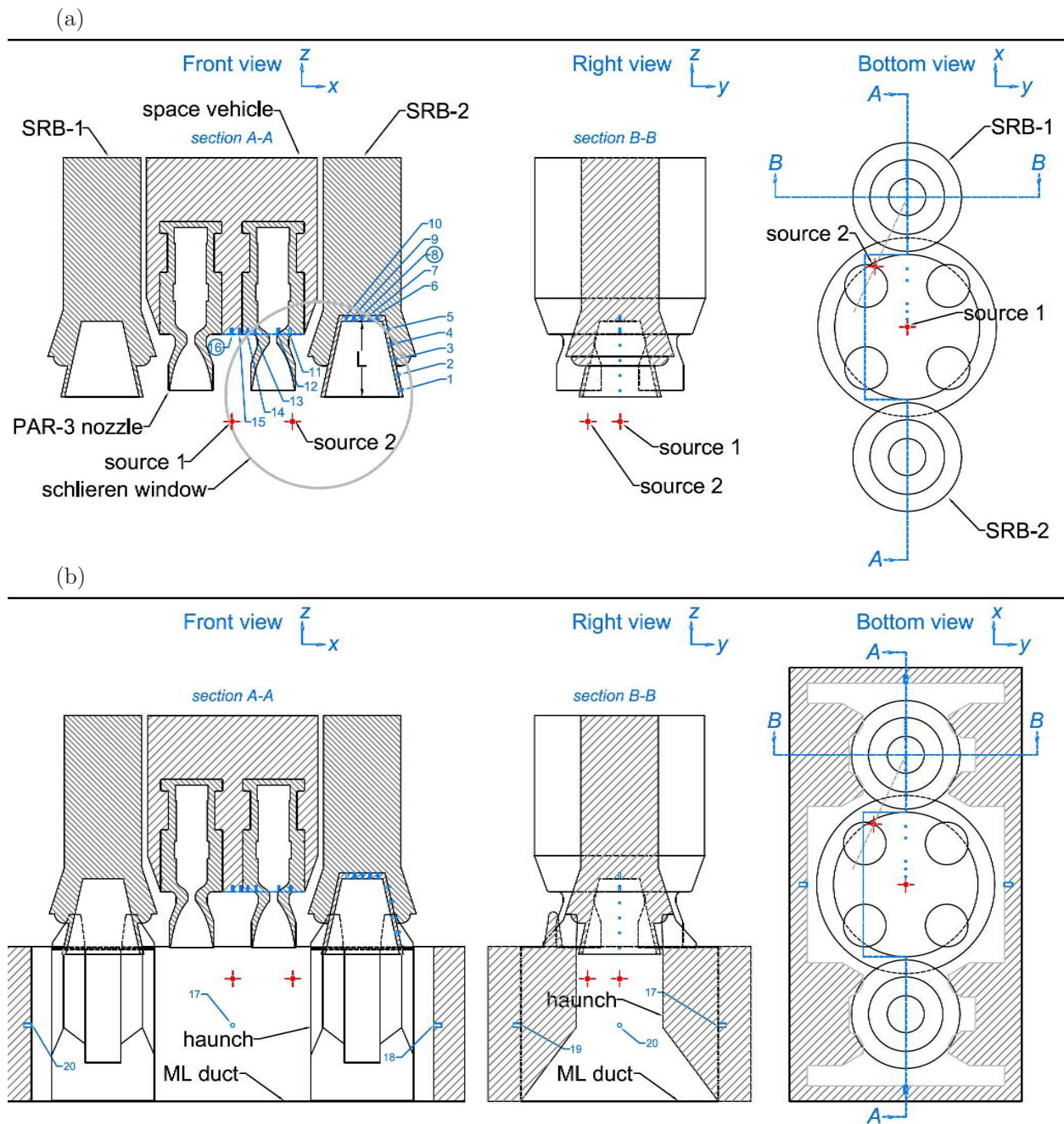
American Institute of Aeronautics and Astronautics

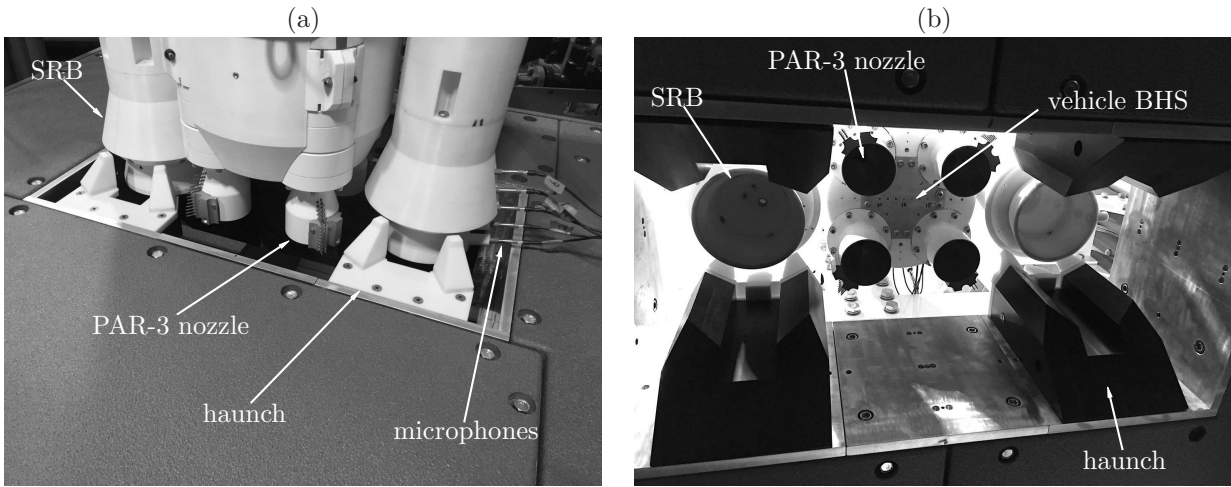Figure 5: Space vehicle test apparatus (a) without and (b) with the mobile launcher.

Figure 6: Test apparatus with ML installed. (a) View from above and (b) below the ML duct.

B. Vehicle Pressure Loads

Pressure waveforms measured on the space vehicle surfaces and ML duct walls are now discussed. Each setup comprises a total of five independent surveys of the microphones at all 20 ports. A comparison of the five tests, to that of their average, is shown in Fig. 9 using sample waveforms from ports 8 and 16 without the ML installed. One can see that differences are within the thickness of the plotted lines and so subsequent analysis is based on waveforms formed by averaging all five independent tests. The x-axis has been initialized by the instant in time when the first pressure rise is sensed at the center of the vehicle BHS (port 16). Close inspection reveals two positive pressure peaks at both sensor ports. The first peak corresponds to the initial pressure wave whereas the second corresponds to the reflected wave, which is of equal or greater strength, relative to the initial wave. The findings are corroborated by the schlieren images presented in Figs. 7 and 8.

Raw pressure time series for both source locations are shown in Fig. 10 without the ML installed (p_1 through p_{16}) and with the ML installed (p_1 through p_{20}). As was done in Fig. 9, the time axis has been initialized by the instant in time when the first pressure rise is sensed at the center of the vehicle BHS (p_{16}). Subsequent waveforms are shifted by 0.20psi in order to reduce clutter. Open and closed symbols identify the first pressure rise (corresponding to the initial wavefront) and the maximum absolute pressure (corresponding to either the initial wavefront or a reflected wavefront), respectively. The maximum absolute pressure can either be negative or positive. Make note of the fact that the maximum absolute pressure does not necessarily correspond to the first peak pressure. This would correspond to instances when the reflected wave has a greater amplitude relative to the initial wave. If open and closed symbols overlap then the initial wavefront is the maximum absolute pressure experienced at that port.

Differences among ports in the arrival times of the first pressure rise coincide with the geometrical disposition of the various sensing ports relative to the spark source locations. For example, in Fig. 10a without the ML installed and for source location 1, port 16 (BHS center) is the first to sense the initial pressure wave while port 6 (farthest port on the SRB throat plug) is the last. With the ML installed and for source location 2 in Fig. 10d, port 11 (outermost port on the vehicle BHS) is the first to sense the initial pressure wave while port 6 is the last. As for the presence of the ML, the arrival times of the initial and reflected waves appear to be unaffected when the source is located at position 1 (comparing Fig. 10a to Fig. 10c). On the contrary, for source location 2 in Fig 10b,d the ML is shown to decrease the time required for the initial wave to impact the SRB nozzle wall ports. It is postulated that the starting wave produced by this spark source (the spark source emits a shock wave that transforms into a propagating acoustic wave), is confined by the ML duct and haunches. If mass and entropy conservation laws are preserved, then this shock is forced to accelerate along available pathways. This appears only to be the case for source location 2, which is when the spark source is closer in proximity to the SRB haunches (see Fig. 5b).
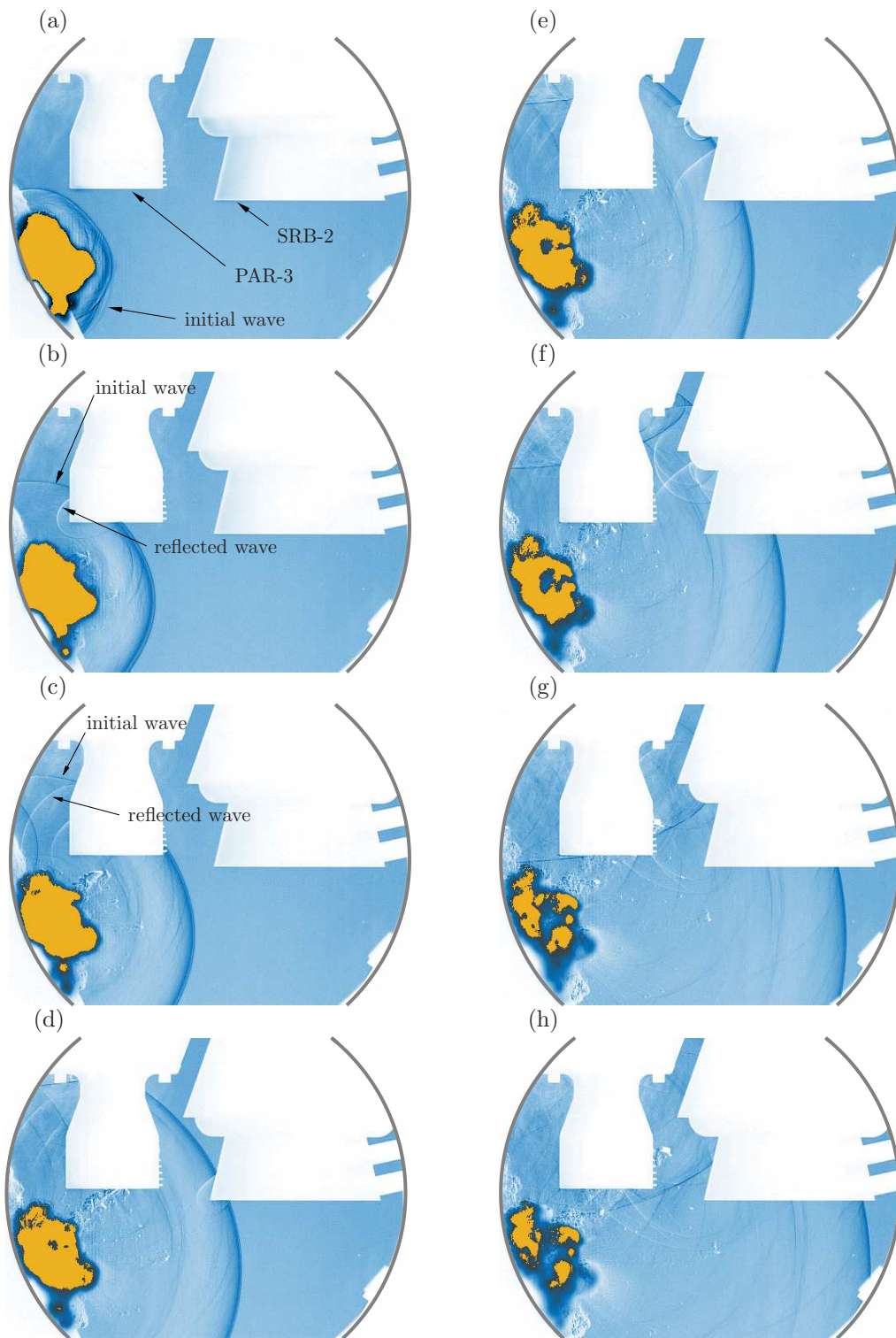
Figure 7: Sparse sequence of schlieren images of a grain based explosive at source location 1 captured at 75,000 fps. (a) $t = t_0 + 13\delta t$ [s], (b) $+19\delta t$ [s], (c) $+25\delta t$ [s], (d) $+33\delta t$ [s], (e) $+36\delta t$ [s], (f) $+41\delta t$ [s], (g) $+51\delta t$ [s], and (h) $+55\delta t$ [s].
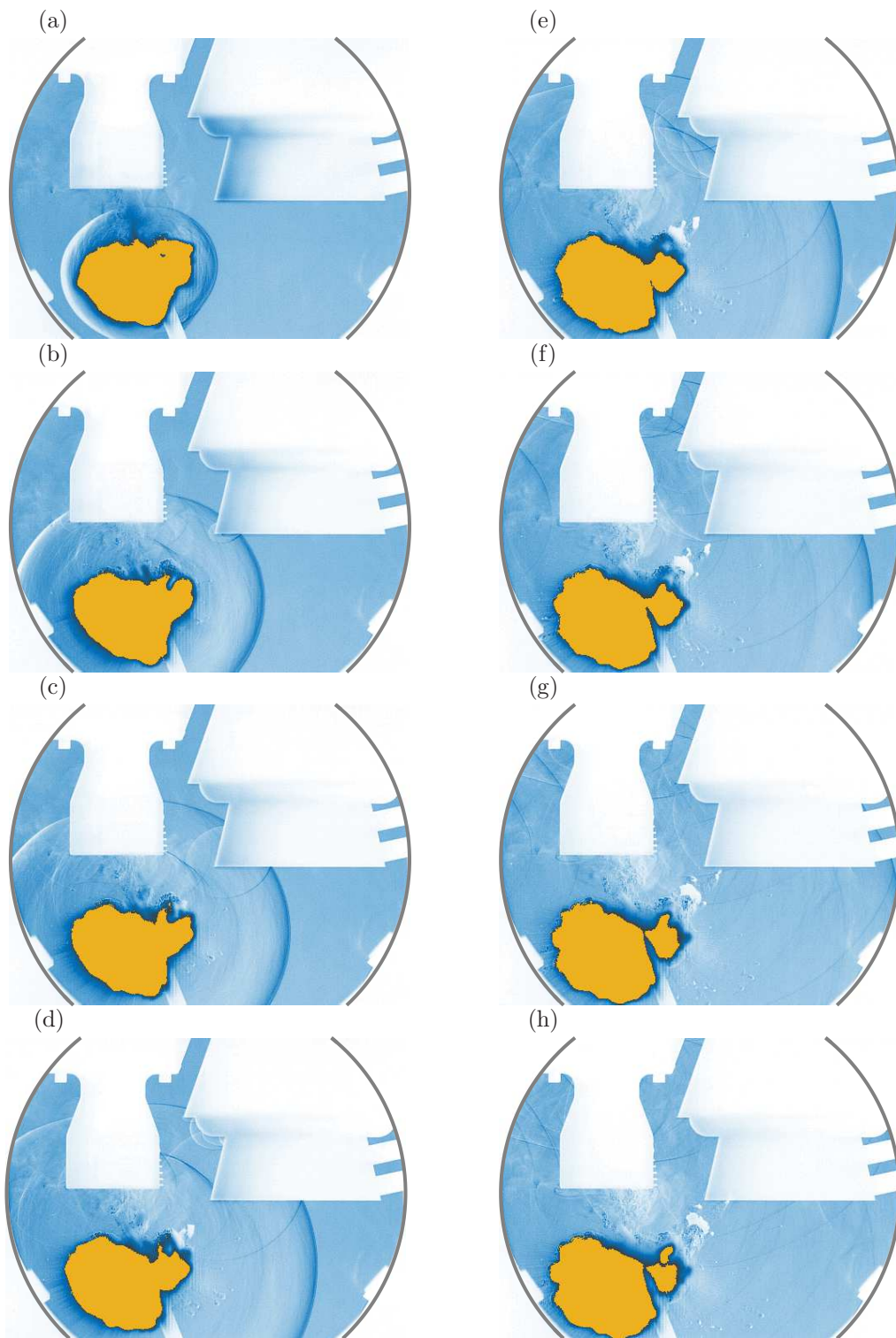
American Institute of Aeronautics and Astronautics

Figure 8: Sparse sequence of schlieren images of a grain based explosive at source location 2 captured at 75,000 fps. (a) $t = t_0 + 9\delta t$ [s], (b) $+16\delta t$ [s], (c) $+20\delta t$ [s], (d) $+25\delta t$ [s], (e) $+30\delta t$ [s], (f) $+35\delta t$ [s], (g) $+40\delta t$ [s], and (h) $+45\delta t$ [s].

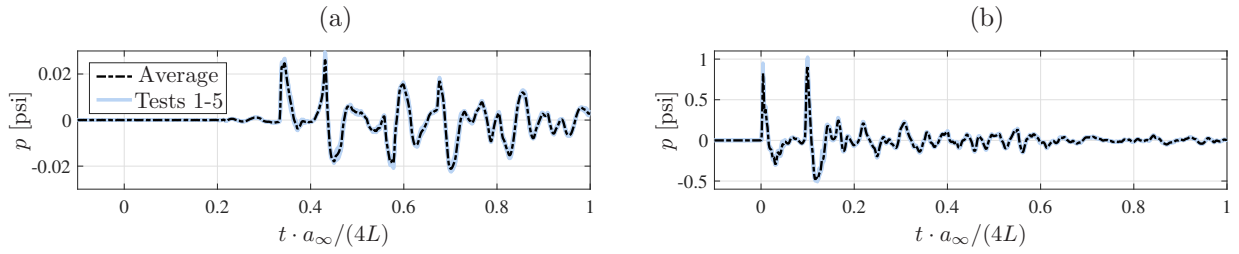American Institute of Aeronautics and Astronautics

Figure 9: Averaging effects using measurements at (a) p_8 and (b) p_{16} for source location 1 without the ML installed.
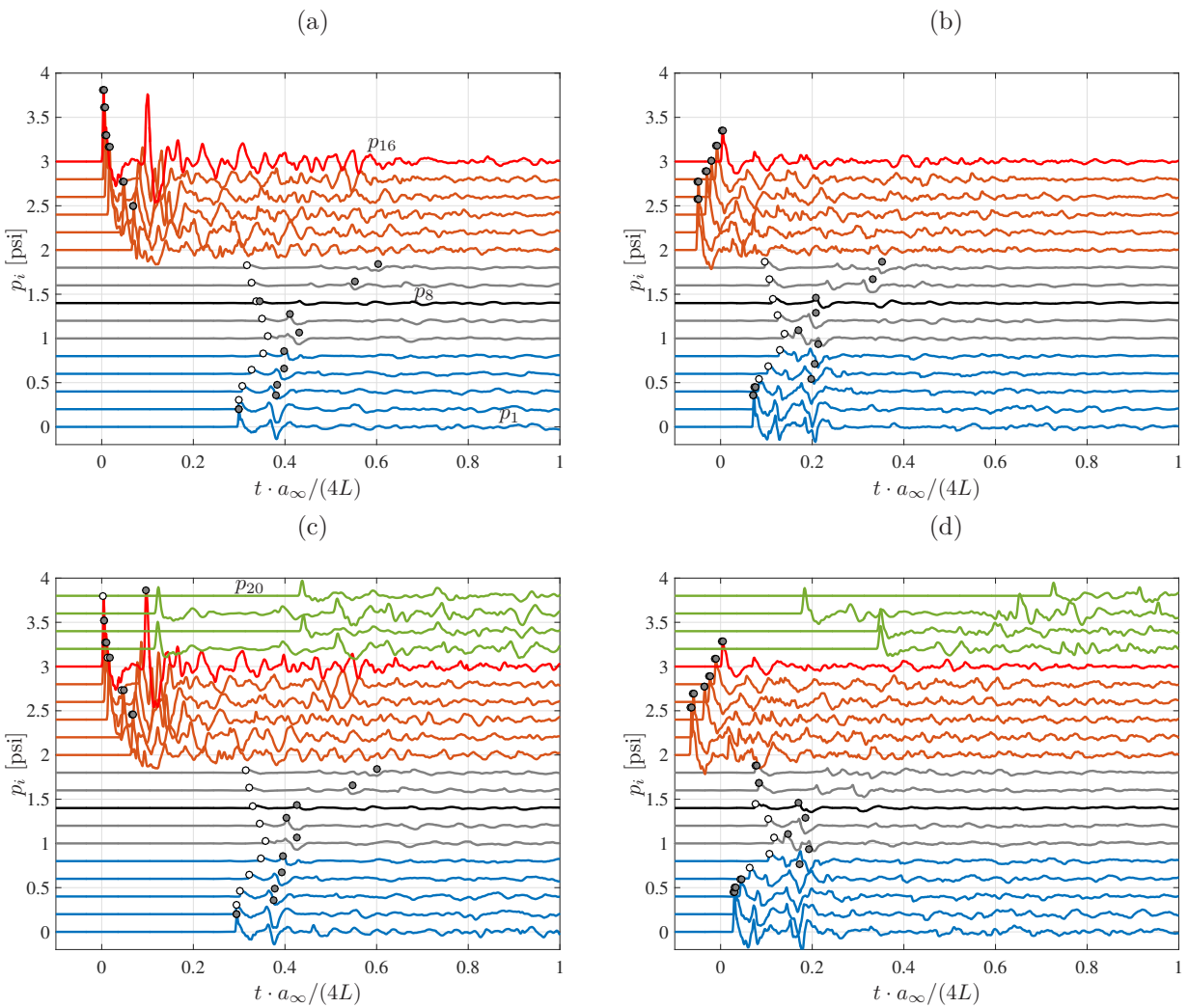

Figure 10: Raw pressure time series for p_1 through p_{16} without the ML installed for (a) source location 1 and (b) source location 2. Ports p_1 through p_{20} with the ML installed for (c) source location 1 and (d) source location 2.

American Institute of Aeronautics and Astronautics

As for the four microphones installed in the ML duct (ports 17 through 20), the raw pressure waveforms confirm the placement and symmetry of the spark source, where the first location of the spark source is concerned. That is, pressure waveforms measured at ports 17 and 19 are identical, while the same is true for waveforms measured at ports 18 and 20. For the second spark source location, which is off-center relative to the model space vehicle and ML duct, The pressure wave is first sensed at port 19, followed by ports 17 and 18, and then eventually picked up at port 20.

Closer inspection of the arrival times and amplitudes of the peak pressures for the ports located on the space vehicle is provided in Fig. 11 by replotting the open and closed symbols from Fig. 10. Pressure amplitudes in Fig. 11b,d have been normalized by the maximum absolute pressure at the center of the vehicle BHS (port 16). Once again, the analysis is confined to the first peak pressure amplitude in Fig. 11a,b, followed by the maximum absolute pressure amplitude (positive or negative) in Fig. 11c,d and is shown for all four configurations (two source locations with and without the ML installed). For both source locations, the initial wavefront produces the largest peak pressure amplitudes on the space vehicle base. On the contrary, reflected waves produce the largest peak pressure amplitudes along the SRB nozzle wall and throat plug plane. As demonstrated in Fig. 11b,d, pressure amplitudes along the SRB nozzle wall and throat are less than 25% of the peak pressure amplitudes measured at the BHS center for source location 1. It is not surprising to see that the pressure amplitudes are greatest at the BHS center and outer regions of the space vehicle when the spark generator is located directly underneath at source 1 and 2, respectively.
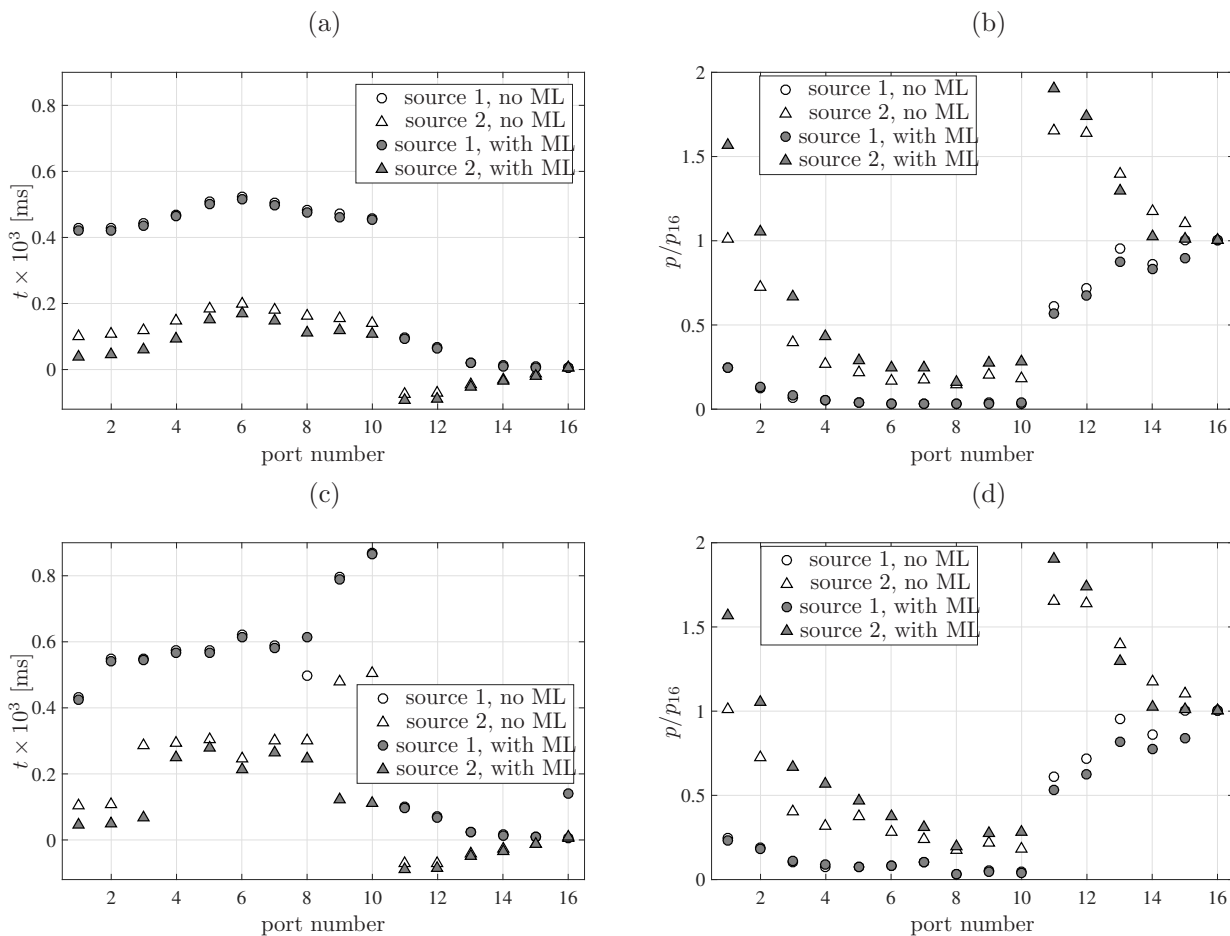

Figure 11: (a) Time lag and (b) normalized pressure value of the first pressure rise relative to the pressure rise at p_{16}. (c) Time lag and (d) normalized pressure value of the maximum pressure relative to the max pressure at p_{16}.

American Institute of Aeronautics and Astronautics

C. Standing Wave Patterns and Spectral Analysis

While much of this discussion has been focused on peak pressure amplitudes, spectral characteristics are equally valuable. Of particular interest is the so-called ring down effect that can form inside the SRB nozzle due to the formation of a standing wave whose length is equal to four times the length of the nozzle ($4L$). Ring down does not appear in Fig. 10 because waveforms are saturated by the large amplitude pressures spikes generated by the initial and reflected waves. Therefore, an enlarged view of one of the waveforms captured inside the SRB nozzle (p_8) is provided in Fig. 12 in order to visualize the extent of this ring down event. The illustration demonstrates how the amplitude of this quarter wavelength event is approximately one order of magnitude less than the peak pressure at this location, but persists for several wavelengths. For both source locations tested, the effect of the ML is to decrease the signal to noise ratio of this quarter wavelength event.
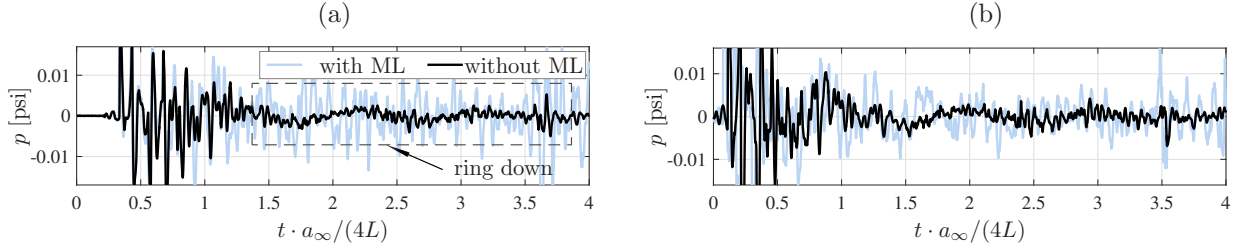

Figure 12: Close up of p_8 with and without ML installed. (a) Source location 1. (b) Source location 2.

Because these signals are transient, it is preferred that one use time-frequency analysis to extract the spectral content associated with these waveforms. In this case, wavelet power spectra are computed, which are resourceful methods for quantifying the frequency content associate with transient unsteady signals.[7, 19, 20] In short, the transform convolves a mother wavelet $\psi(t/l)$ with an arbitrary waveform $p(t)$ in order to produce wavelet coefficients. Here, the Morlet wavelet is selected and is defined as $\psi(t/l) = e^{j\omega_\psi t/l} e^{-|t/l|^2/2}$ with a central frequency of $\omega_\psi = 6$. The transform is performed in the Fourier domain using 98 different scales (l) distributed logarithmically across the frequency range 290 Hz $< f < f_s/2$. Only regions inside the cone of influence are valid and so the transform must be initiated before the arrival of the initial waveform. The energy density is thus determined by,

$$E(l,t) = \frac{|\tilde{p}(l,t)|^2}{l}, \tag{1}$$

and is obtained using complex-valued wavelet coefficients $\tilde{p}(l,t)$ defined as,

$$\tilde{p}(l,t) = \int p(t') \bar{\psi}\left(\frac{t'-t}{l}\right) dt. \tag{2}$$

Wavelet power spectra (WPS) are generated using data acquired at ports 8 (center of the SRB throat plug) and 16 (vehicle BHS center) for both source locations, and with and without the ML installed. The findings are illustrated in Fig. 13. Without the ML installed, the WPS in Fig. 13a,b reveal a noticeable tone in the SRB nozzle corresponding to the quarter wave event which also persists for several wavelengths. With the ML installed, the quarter wave tone is much less noticeable as seen in Fig. 13c,d. At the center of the BHS in Fig. 13e-f, the spectral content is much more broadband for all conditions studied. A weak low frequency tone appears for source location 2 in Fig. 13f,h with a frequency that is twice the quarter wavelength.

Acknowledgments

References

[1]Tang, M. J., and Baker, Q. A., "A new set of blast curves from vapor cloud explosions," *Process Safety Progress,* Vol. 18, No. 3, Winter 1999, pp. 235-240.
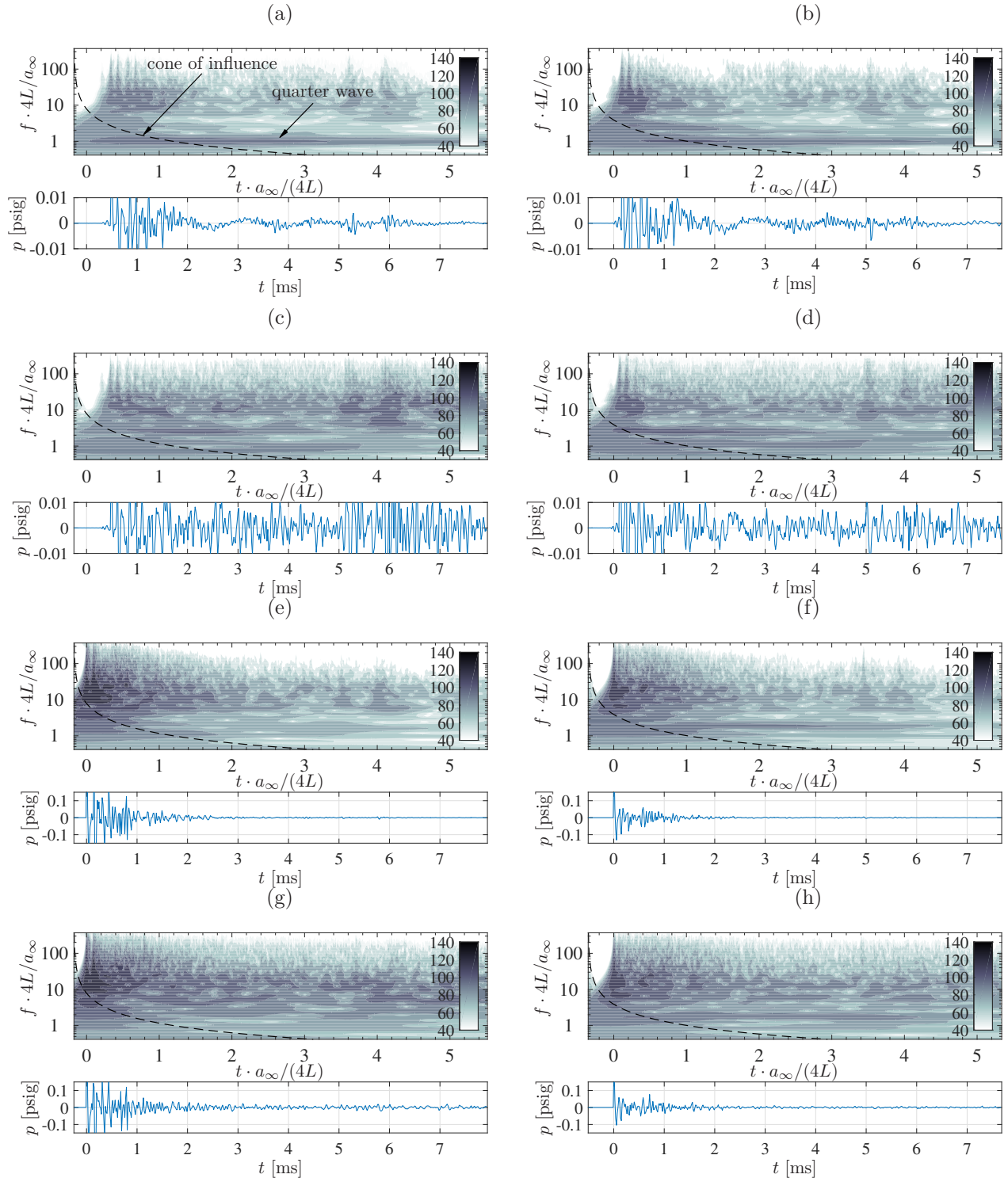
Figure 13: Morlet wavelet power spectra of p_8 expressed as $10 \log_{10}(E(f,t)/\text{ref}^2)$ [dB, ref: 20 μPa/$\sqrt{\text{Hz}}$] without the ML installed for (a) source location 1 and (b) source location 2 and with the ML installed for (c) source location 1 and (d) source location 2. (e-h) The same setup and analysis for p_{16}.

American Institute of Aeronautics and Astronautics

[2]Melton, T. A., and Marx, J. D., "Estimating flame speeds for use with BST blast curves," *Process Safety Progress,* Vol. 28, No. 1, March 2009, pp. 1-11.

[3]Xu, Y., Worthington, D., and Oke, A., "Correcting the predictions by Baker-Strehlow-Tang (BST) model for the ground effect," *IChemE,* Symposium Series No. 155, Hazards XXI, 2009, pp. 318-325.

[4]Allgood, D. C., "Development of detonation modeling capabilities for rocket test facilities: Hydrogen-Oxygen-Nitrogen mixtures," *NASA/TP-2016-219220,* April 2016, pp. 1-57.

[5]Brossard, J., Hendricks, S., Garnier, J. L., Lannoy, A., and Perrot, J. L., "Air blast from unconfined gaseous detonations," *Dynamics of Shock Waves, Explosions, and Detonations* Progress in Astronautics and Aeronautics, Presented at the 9th ICODERS, Poitiers, France July 3-8, 1983.

[6]Valdez, J., and Tinney, C. E., "Measurements of a Mach 3 jet using high-speed optical flow techniques," *AIAA/CEAS Aeroacoustics Conference,* AIAA Paper 2018-3148, June 25-29, 2018.

[7]Baars, W. J., and Tinney, C. E., "Transient Wall Pressure in an Overexpanded and Large Area-Ratio Nozzle," *Experiments in Fluids,* Vol. 54:1468, Feb. 2013, pp. 1-17.

[8]Donald, B. W., Baars, W. J., Tinney, C. E., and Ruf, J. H., "Sound produced by large area-ratio nozzles during fixed and transient operations," *AIAA Journal,* Vol. 52, No. 7, 2014, pp. 1474-1485.

[9]Kleeman, D. R., "Development and use of a schlieren system for sound pulse studies," *Air Force Office of Scientific Research*, AFOSR-TR-77-0679, August 1976.

[10]Cobb, W. N., "Diffraction of a plane N wave of finite amplitude by a slit," Air Force Office of Scientific Research, AFOSR-TR-78-0149, August 1977.

[11]Lipkens, B., "Experimental and theoretical study of the propagation of N waves through a turbulent medium," (PhD thesis), The University of Texas at Austin, Austin, TX 1993.

[12]Lipkens, B., Blackstock, D. T., "Model experiment to study sonic boom propagation through turbulence. Part I: General results," *J. Acoustical Society of America,* Vol. 103, Issue 1, January 1998.

[13]Weinstein, L. M., "Large-Field High-Brightness Focusing Schlieren System", *AIAA Journal,* Vol. 31, No. 7, 1993, pp. 1250-1255.

[14]Settles, G. S. "Schlieren and Shadowgraph Techniques." *Experimental Fluid Mechanics,* Springer-Verlag, Ch. 6., 2001.

[15]Garg, S., and Cattafesta, L. N. "Quantitative schlieren measurements of coherent structures in a cavity shear layer." *Experiments in Fluids,* Vol. 30, 2001, pp. 123-134.

[16]Hargather, M. J., and Settles, G. S. "Retroreflective shadowgraph technique for large scale flow visualization." *Applied Optics,* Vol. 48, No. 22, 2009, pp. 4449-4457.

[17]Mitchell, D. M., Honnery, D. R., and Soria, J. "The underexpanded jet Mach disk and its associated shear layer." *Physics of Fluids,* Vol. 26, No. 096101, 2014.

[18]Canchero, A., Tinney, C. E., Murray, N., and Ruf, J. H., "Flow and Acoustics of Clustered Rockets During Startup" , *AIAA Journal,* Vol. 54, No. 5, 2016, pp. 1660-1670.

[19]Farge, M., "Wavelet transforms and their application to turbulence," *Annual Review of Fluid Mechanics,* Vol. 24, Jan. 1992, pp. 395-458.

[20]Addison, P. S., "The illustrated wavelet transform handbook," *Taylor & Francis Group, New York,* 2002.